J Comp Physiol A (2005) 191: 331–345
DOI 10.1007/s00359-004-0587-3

ORIGINAL PAPER

Ling Chen · Jonathan L. House · Rüdiger Krahe
Mark E. Nelson

Modeling signal and background components of electrosensory scenes

Received: 18 August 2004 / Revised: 26 October 2004 / Accepted: 5 November 2004 / Published online: 17 December 2004

Abstract Weakly electric fish are able to detect and localize prey based on microvolt-level perturbations in the fish's self-generated electric field. In natural environments, weak prey-related signals are embedded in much stronger electrosensory background noise. To better characterize the signal and background components associated with natural electrolocation tasks, we recorded transdermal voltage modulations in restrained *Apteronotus albifrons* in response to moving spheres, tail bends, and large nonconducting boundaries. Spherical objects give rise to ipsilateral images with center-surround structure and contralateral images that are weak and diffuse. Tail bends and laterally placed nonconducting boundaries induce relatively strong ipsilateral and contralateral modulations of opposite polarity. We present a computational model of electric field generation and electrosensory image formation that is able to reproduce the key features of these empirically measured signal and background components in a unified framework. The model comprises an array of point sources and sinks distributed along the midline of the fish, which can conform to arbitrary body bends. The model is computationally fast and can be used to estimate the spatiotemporal pattern of activation across the entire electroreceptor array of the fish during natural behaviors.

L. Chen · J. L. House · R. Krahe · M. E. Nelson
Beckman Institute for Advanced Science and Technology,
University of Illinois at Urbana-Champaign,
405 N. Mathews Ave., Urbana, IL 61801, USA

R. Krahe · M. E. Nelson (✉)
Department of Molecular and Integrative Physiology, University of Illinois at Urbana-Champaign, Urbana, IL 61801, USA
E-mail: m-nelson@uiuc.edu
Tel.: +1-217-2441371
Fax: +1-217-2445180

Present address: R. Krahe
Department of Biology, McGill University, Montreal,
H3A1B1, Canada

Keywords Electric organ · Electrolocation · Electroreception · Natural scenes · Prey capture

Abbreviations ELL: Electrosensory lateral line lobe · EOD: Electric organ discharge · FWHM: Full-width at half-maximum · RMS: Root mean square · SNR: Signal-to-noise ratio

Introduction

Over the course of evolution, the processing properties of sensory systems have been shaped by the necessity of extracting behaviorally relevant information from naturally occurring sensory input (Dusenbery 1992). Since the pioneering works of Attneave (1954) and Barlow (1961), investigators have been interested in formulating, testing, and refining hypotheses of how sensory systems are adapted to natural sensory input. An important thrust of recent work in this area has been careful quantitative analysis of natural sensory inputs, particularly in visual and auditory modalities (e.g. Field 1987; Ruderman and Bialek 1994; Rieke et al. 1995). Here we describe a set of experimental and modeling studies that provide insight into the properties of natural electrosensory scenes experienced by weakly electric fish.

While auditory and visual scene analysis can take advantage of modern digital audio and video recording techniques, there is currently no corresponding technology for conveniently recording natural electrosensory images. Consequently, we have taken a computational approach that utilizes an empirically constrained model of electrosensory image formation to predict spatiotemporal input patterns across a broad range of behaviorally relevant conditions. The approach has two components: measurement of naturalistic electrosensory input at a small number of locations on the fish under restrained conditions, and development of a model capable of predicting electrosensory input over the entire body surface under free swimming conditions.

This paper presents the computational model and associated empirical data that were used to calibrate and test the model. Although the work presented here is restricted to the analysis of individual scene components, rather than entire scenes, the modeling framework should provide a useful tool for future studies addressing the full spatial and temporal structure of electrosensory images in naturalistic environments.

Weakly electric fish generate electric fields by discharging an electric organ typically found in the tail region (Bass 1986). The species studied here, *Apteronotus albifrons*, has a quasisinusoidal, wave-type electric organ discharge (EOD) waveform, with a discharge frequency in the range of 800–1300 Hz. The field has an approximately dipolar spatial structure (Knudsen 1975). Nearby objects, such as rocks, plants, and prey, perturb the electric field. These perturbations are monitored by tuberous electroreceptor organs distributed over the skin of the fish (Zakon 1986). The active electrosensory system allows the fish to detect, identify, and localize objects in its environment even in complete darkness (Lissmann 1958; Bastian 2003). While much is known about electric field properties (Assad et al. 1999), peripheral and central processing of electrosensory stimuli (Heiligenberg 1991; Gabbiani and Metzner 1999; Berman and Maler 1999), and prey image characteristics (Nelson and MacIver 1999), little information is available about the composition of natural electrosensory scenes and the relative contributions of different scene components to the net electrosensory signal.

Methods

Animals

Adult weakly electric fish ($n = 13$) of the species *A. albifrons* (black ghost knife fish), 17–24 cm in length, were used in this study. Fish were housed in laboratory aquaria, measuring 30×60×30 cm with one to six fish per tank, and were kept on a 12:12 h light:dark cycle at a temperature of 28 ± 2°C. Water conductivity of the home tanks was 120 ± 20 μS cm^{-1} and the pH was 7.0 ± 0.5.

Transdermal recordings

The voltage across the skin (transdermal potential) was recorded using custom-made electrodes attached to a thin flexible cable. The custom cable was constructed by braiding two strands of insulated magnet wires (38 gauge), which formed the signal path, with one uninsulated strand of bus bar wire (36 gauge) that was grounded for electrical shielding. The braided wires were painted with Silver Print (GE Electronics) to improve shielding and subsequently coated with Insulating Coating (GE Electronics). The resulting three-conductor cable was approximately 0.5 mm in diameter and 80 cm in length. One end of this cable was connected to a differential amplifier (A-M Systems, model 1700) and the other end was attached to the recording electrodes. Transdermal electrodes consisted of two Teflon-coated silver wires (0.20 mm bare, 0.28 mm coated), 2.5 cm in length. The Teflon coating was removed from the distal 1 mm and the tips were chlorided by immersion in bleach. One silver wire was implanted subcutaneously along the longitudinal axis of the fish at the level of the lateral line, while the other silver wire rested against the outside of the fish skin next to the implanted wire. For stability of the recordings, the transdermal cable was sutured to the skin 2 cm proximal to the tips. In most experiments, two transdermal pairs were implanted, one on either side of the fish's trunk. The rostro-caudal positioning was such that the chlorided tips of the electrodes were located approximately 30–40% of the body length from the snout. Signals were amplified (gain = 1,000) and bandpass filtered between 300 Hz and 5 kHz. Signals were sampled at 40 kHz with a digital data acquisition card (NI6035, National Instruments) and stored on magnetic disk.

Fish were anesthetized by immersion in 100 ppm tricaine methanesulfonate (MS-222, Sigma) prior to implantation of the transdermal electrodes. Fish were then immobilized by injection of 6–12 µl of 10% gallamine triethiodide (Flaxedil, Sigma) and artificially respirated with a constant flow of aerated water across the gills (3 ml/min). The electric organ discharge from the neurogenic organ remained intact following Flaxedil injection. Fish were allowed to recover for 30–60 min after surgery before transdermal signals were recorded. The fish was strapped in a holder and positioned in the center of a large cylindrical 1,375-l tank, 175 cm in diameter and 60 cm in height. The holder was designed to minimize perturbations of the fish's electric field; it consisted of two vertical, foam-padded Plexiglas bars (4 mm wide, 2 mm thick, 6 cm high) on the side of the fish contralateral to the object movement. One bar was located just behind the pectoral fin and the second one at approximately 65% of the body length from the head. A single strand of polyethylene tubing (1 mm outside diameter) was used to gently strap the fish against each support bar; the tubing was the only material on the ipsilateral side of the fish. The fish was placed at a depth of approximately 30 cm below the surface. A stepper-motor-controlled robotic positioning device (MD2, Arrick robotics) was used to move objects or field gradient electrodes precisely (0.013 cm resolution) around the fish. The positions of the head, tail, and transdermal electrode sites were calibrated relative to the origin of plotter movements.

The transdermal potential was monitored under baseline conditions and in the presence of nonconducting boundaries, small spherical objects, and during tail bending. The nonconducting boundary was a vertically oriented Plexiglas plate (31 L×20 H×0.5 W cm) placed parallel with the rostro-caudal axis of the fish at fixed distances. Lateral tail bends were imposed by moving

the plotter with a short monofilament nylon line attached from the plotter arm to the tip of the tail. The rostral portion of the body (approximately 65% of the body length) was constrained by the fish holder to remain in a straight line, while the caudal portion (approximately 35%) was allowed to bend. The bend angle was defined by the angle from the pivot point to the tip of the tail. The plotter moved the tail through a series of angles ranging from −45° through 45°. The tip of the tail was positioned to fall on the arc of a circle with a radius of curvature R that was inversely proportional to the bend angle: $R = L/2\theta$, where θ is the bend angle in radians and L is the length of the tail that was allowed to bend.

The effects of small objects were quantified by moving conductive (metal) or resistive (plastic) spheres of different diameters (1.91, 1.27, and 0.635 cm) parallel to the rostro-caudal axis of the fish at different lateral distances. For the six object types, four sweeps were made at each distance, alternating between head-to-tail and tail-to-head. The sweeps extended from approximately 5 cm in front of the head to 5 cm beyond the tail. The speed of the movement was 2.5 cm/s. Spheres were attached to the tip of a wooden "L-shaped" dowel rod to minimize the effect of the object holder on the transdermal potential.

Electric field recordings

The lateral component of the electric field was measured by positioning a dipolar recording electrode next to the skin and moving it transversely in discrete steps up to a distance of approximately two body lengths from the fish midline. The recording electrode was constructed from a pair of glass capillary tubes (OD = 0.12 cm) spaced 0.96 cm apart. Each capillary contained an insulated silver wire with an exposed tip that had been heated to form a small silver ball (150–250 μm diameter). The dipolar electrode was positioned in the horizontal midplane of the fish with the recording tips along a line perpendicular to the midline, such that the electrode monitored the lateral gradient in the trunk region.

Data analysis

Amplitude envelopes of the oscillatory transdermal potential and field gradient recordings were extracted by first bandpass-filtering (third-order Butterworth) the signal between ±100 Hz of the fish's EOD frequency and then applying the Hilbert transform (Haykin 2001). The envelope was low-pass filtered (third-order Butterworth) with a cutoff of 100 Hz, subsampled at 2 kHz, and linearly detrended.

The amplitude modulation induced when a small sphere is moved past the fish has a "Mexican-hat" shape (Caputi et al. 1998) that can be described by a difference of Gaussians. A nonlinear least-squares fit to the data was carried out using the following functional form:

$$A(t) = A_c \exp\left[-\frac{(x(t)-x_c)^2}{2\sigma_c^2}\right] + A_s \exp\left[-\frac{(x(t)-x_s)^2}{2\sigma_s^2}\right] + C, \quad (1)$$

where $A(t)$ is the envelope amplitude, $x(t)$ is the rostro-caudal location of the sphere, A_c, x_c, σ_c^2, A_s, x_s, and σ_s^2, are the amplitudes, center locations, and width parameters of the center and surround Gaussians, and C is a constant offset which was usually negligible (Fig. 1a, b). The best-fit parameters were obtained for each of the four sweeps of a given object at each distance. Data records from all sweeps were visually inspected and those containing abrupt EOD frequency shifts ("chirps") or large voltage drifts were discarded.

We estimate that systematic errors of up to 0.2 cm occurred during the visual calibration of the transdermal electrode position relative to the object coordinate system. This offset could be estimated using the y-intercept of the linear fit to image width versus object distance (see Results, Fig. 8c, d) resulting in a lateral position correction for each experimental session of up to ±0.2 cm. Applying this correction reduced the variance of the population averages without significantly shifting their means. Table 1 reports both corrected and uncorrected parameter values. All other figures and values reported here are based on uncorrected data.

Electric field model

The electric field of *A. albifrons* was modeled using n electric poles uniformly distributed along the rostro-caudal axis of the model fish. Within an EOD cycle, the electric potential alternates between head-positive and tail-positive, resulting in a quasi-sinusoidal signal. For computational efficiency, we modeled only a single time point in the EOD cycle when the head is maximally positive (Fig. 2a). Of the n poles in the model fish, the first m poles starting at the head act as a current source and the remaining $(n-m)$ poles, at the tail of the fish, act as a current sink.

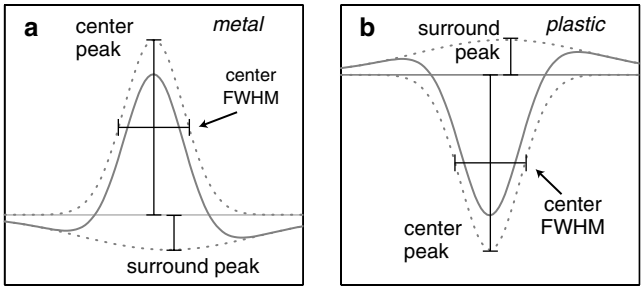

Fig. 1 Schematic diagram of the parameterized components of the temporal voltage modulation profile for both **a** metal and **b** plastic objects. The difference-of-Gaussians waveform (*solid line*) is fit to the sum of "center" and "surround" Gaussians (*dotted lines*). The center peak, surround peak, and center full-width at half-maximum (*FWHM*) are indicated

Table 1 Summary of power-law fits to experimental data for metal and plastic spheres ($n = 7$ fish for 1.91 and 1.27 cm spheres, $n = 3$ fish for 0.635 cm spheres)

Component	p	Metal			Plastic		
		$A_{1.91}$	$A_{1.27}$	$A_{0.635}$	$A_{1.91}$	$A_{1.27}$	$A_{0.635}$
Center	-4.7 ± 0.4	568 ± 520	136 ± 124	13 ± 9	-397 ± 298	-121 ± 102	-11 ± 4.9
Center (adj)	-4.8 ± 0.2	572 ± 203	137 ± 49	16 ± 1.4	-431 ± 158	-129 ± 66	-14 ± 1.5
Surround	-4.6 ± 0.8	43 ± 50	11 ± 13	0.8 ± 0.4	-21 ± 23	-6.7 ± 8.7	-0.4 ± 0.1
Contralateral	-3.7 ± 0.5	11 ± 7.5	2.1 ± 0.6	0.3 ± 0.1	-7.5 ± 3.1	-2.0 ± 0.5	-0.4 ± 0.2

The peak percent changes A_{peak} observed in center, surround, and contralateral recordings are fit with the form $A_{\text{peak}}(d) = Ad^p$, where A is a scaling factor (%), d is the lateral distance from the object center to the fish midline (cm) and p is the power-law exponent. Within a category (center, surround, or contralateral), a single power-law exponent is used across all objects (i.e., the power-law curves are constrained to have the same slope), but each object size and type have their own A value. Small lateral distance corrections were applied to the row labeled "center (adj)" (see Methods)

The electric potential ϕ (mV) at a point $\mathbf{x}$ (cm) in the water outside of the fish is given by the sum of the individual contributions to the potential from each pole:

$$\phi(\mathbf{x}) = \sum_{i=1}^{m} \frac{q/m}{\left|\mathbf{x} - \mathbf{x}_p^i\right|} - \sum_{i=m+1}^{n} \frac{q/(n-m)}{\left|\mathbf{x} - \mathbf{x}_p^i\right|}, \quad (2)$$

where $\mathbf{x}$ is a point in space, $\mathbf{x}_p^i$ the location of pole i, and q is a normalization constant (mV cm) that scales the overall magnitude of the potential. The quantity q is analogous to electric charge in an electrostatic model and is distributed such that the first m poles have a "charge" of q/m and the remaining poles have a charge of $-q/(n-m)$, resulting in a total net charge of zero.

Model parameters

The free parameters of the model are n (total number of poles), m (number of positive poles), q (normalization constant), and $\mathbf{x}_p^i$ (3D location of each pole). For *A. albifrons*, we found that the field was well described using a uniform distribution of poles along the entire length of the fish, with a single negative pole at the tail (see Results). For fish of different lengths, the total number of poles n was adjusted to maintain a constant density of 10 poles/cm and the normalization constant q was matched to each individual fish. In summary, the parameter values used in our model are as follows:

- n: approximately 200 poles (10 poles/cm, varies with fish length)
- m: $n-1$ ($n-1$ positive poles, one negative pole)
- q: fish dependent (about 8 mV cm for small fish to 20 mV cm for large fish)
- $\mathbf{x}_p^i$: poles are uniformly distributed along the midline from head to tail

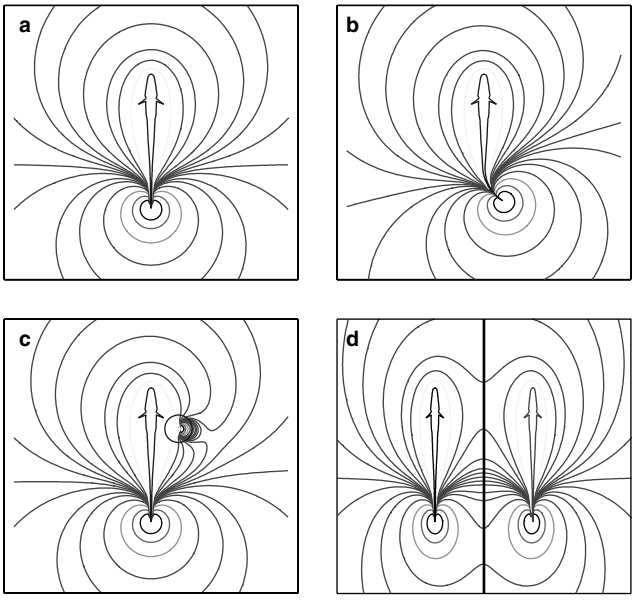

Fig. 2 Sample model configurations and modeled isopotential contours for conditions used in this study: **a** straight body, **b** bent tail, **c** conducting spherical object, and **d** planar nonconducting boundary. The fish on the *right-hand side* of **d** is the reflected "mirror" fish (see Methods)

Electric field and transdermal calculations

The electric field vector $\mathbf{E}$ at a point $\mathbf{x}$ is the negative gradient of the electric potential ϕ:

$$\mathbf{E}(\mathbf{x}) = -\nabla\phi(\mathbf{x}) = -\frac{\partial\phi(\mathbf{x})}{\partial x}\hat{\mathbf{x}} - \frac{\partial\phi(\mathbf{x})}{\partial y}\hat{\mathbf{y}} - \frac{\partial\phi(\mathbf{x})}{\partial z}\hat{\mathbf{z}}, \quad (3)$$

where $\hat{\mathbf{x}}$, $\hat{\mathbf{y}}$, and $\hat{\mathbf{z}}$ are the unit vectors in the respective directions. In the model, the partial derivative does not need to be computed numerically since there is an analytic solution:

$$\mathbf{E}(\mathbf{x}) = \sum_{i=1}^{m} \frac{q/m}{\left|\mathbf{x} - \mathbf{x}_p^i\right|^3}\left(\mathbf{x} - \mathbf{x}_p^i\right) - \sum_{i=m+1}^{n} \frac{q/(n-m)}{\left|\mathbf{x} - \mathbf{x}_p^i\right|^3}\left(\mathbf{x} - \mathbf{x}_p^i\right). \quad (4)$$

The transdermal potential difference across the fish skin, $V_{\text{td}}(\mathbf{x}_s)$, is computed as

$$V_{\text{td}}(\mathbf{x}_s) = \mathbf{E}(\mathbf{x}_s) \cdot \hat{\mathbf{n}}(\mathbf{x}_s)\frac{\rho_{\text{skin}}}{\rho_{\text{water}}}, \quad (5)$$

where $\mathbf{x}_s$ is a point on the surface of the fish, $\mathbf{E}(\mathbf{x}_s)$ is the electric field in the water just outside the surface, $\hat{\mathbf{n}}(\mathbf{x}_s)$ a

unit vector normal to the skin at that point, and ρ_{skin} is the specific resistivity of the skin (kΩ cm^2) and ρ_{water} is the bulk resistivity of the water (kΩ cm) (see Rasnow 1996). Estimates of the skin resistivity range from approximately 1–7 kΩ cm^2 (Scheich and Bullock 1974; Rasnow 1996; Assad 1997). Our experiments were conducted in water with a resistivity of 10 kΩ cm, resulting in an estimated resistivity ratio $\rho_{\text{skin}}/\rho_{\text{water}}$ of 0.1–0.7 cm. As discussed below, changes in transdermal potential reported here are expressed in a form that is insensitive to the numeric value of this ratio (see below). We used 3D fish body geometry data from MacIver (2001) for determining surface points and surface normals.

Effects of spherical objects

We modeled the effects of small spherical objects using the induced-dipole approximation (Fig. 2c). For a spherical objected centered at $\mathbf{x}_{\text{obj}}$, the potential perturbation $\delta\phi$ at location $\mathbf{x}$ is

$$\delta\phi(\mathbf{x}) = \chi \frac{a^3 \mathbf{E}(\mathbf{x}_{\text{obj}}) \cdot (\mathbf{x} - \mathbf{x}_{\text{obj}})}{|\mathbf{x} - \mathbf{x}_{\text{obj}}|^3}, \tag{6}$$

where a is the radius of the sphere, $\mathbf{E}(\mathbf{x}_{\text{obj}})$ the electric field vector at the location of the object, and χ is the electrical contrast (Rasnow 1996). The contrast is unity for a perfect conductor, -0.5 for a perfect insulator and zero if the electrical impedance of the sphere matches that of the surrounding water.

In the presence of an object, the change in transdermal potential at a point $\mathbf{x}_s$ on the skin, $\Delta V_{\text{td}}^{\text{obj}}(\mathbf{x}_s)$, is the difference between the transdermal potential in the presence of an object $V_{\text{td}}^{\text{obj}}(x_s)$ and the baseline transdermal potential $V_{\text{td}}^{\text{base}}(x_s)$. This simplifies to

$$\Delta V_{\text{td}}^{\text{obj}}(\mathbf{x}_s) = -\nabla(\delta\phi(\mathbf{x}_s)) \cdot \hat{\mathbf{n}}(\mathbf{x}_s) \frac{\rho_{\text{skin}}}{\rho_{\text{water}}}. \tag{7}$$

The fractional change in transdermal potential is $\Delta V_{\text{td}}^{\text{obj}}(\mathbf{x}_s)/V_{\text{td}}^{\text{base}}(\mathbf{x}_s)$. Note that the resistivity ratio ($\rho_{\text{skin}}/\rho_{\text{water}}$) and overall field strength normalization (q) in the numerator and the denominator will cancel out. Thus, the fractional change in transdermal potential is independent of assumptions regarding the skin-to-water resistivity ratio or the magnitude of the field strength.

Effects of nonconducting boundaries

The effects of nonconducting boundaries (water surface, tank walls, etc.) were modeled using the method of image charges (Jackson 1975). In the presence of a planar nonconducting boundary, the pole locations $\mathbf{x}_p^i$ of the original fish model are duplicated and mirror-reflected in the plane. The resulting potential at a point $\mathbf{x}$ is the sum of the potential from the "original" and "mirrored" fish, $\phi_{\text{wall}}(\mathbf{x}) = \phi_{\text{orig}}(\mathbf{x}) + \phi_{\text{mirror}}(\mathbf{x})$. For a plane defined by $ax + by + cz + d = 0$ with unit normal $\hat{\mathbf{n}}_{\text{plane}} = \langle a, b, c\rangle / |\langle a, b, c\rangle|$, the positions of the mirror fish poles $\mathbf{x}_m^i$ are given by

$$\mathbf{x}_{\text{m}}^i = \mathbf{x}_{\text{p}}^i - 2(\mathbf{x}_{\text{p}}^i \cdot \hat{\mathbf{n}}_{\text{plane}} + d)\, \hat{\mathbf{n}}_{\text{plane}}. \tag{8}$$

The electric field vector in the presence of the wall is computed using an equation similar to Eq. 4, except that the terms are summed over all poles including both the original fish and the mirrored fish. The transdermal potential is then computed using Eq. 5 as before.

General methods

All data analysis and modeling were performed in MATLAB (The Mathworks, Natick, USA). Statistical values are reported as mean ± standard deviation, unless otherwise noted. When comparing the model predictions with the experimental results across n sample points, the RMS percent error is computed as

$$\text{RMS}(\%) = 100 \cdot \sqrt{\frac{1}{n}\sum_{i=1}^{n}\left(\frac{\text{model}_i - \text{expt}_i}{\text{expt}_i}\right)^2}. \tag{9}$$

Results

Spatial structure of the electric field

Far from the fish, the spatial structure of the electric field approximates that of a simple dipole source (Knudsen 1975), but in the near field (< 1 body length), the elongated shape of the fish body and the low internal body resistance affect the pattern of current flow. To model the electric field, we consider two sets of electrical poles placed along the midline of the fish. The positive set of poles is uniformly distributed over a line segment of length L_1 centered at rostro-caudal location X_1, while the negative poles are distributed along a segment of length L_2 centered at X_2. This arrangement is analogous to the line-charge model introduced by Bacher (1983). We fit the model parameters to experimental measurements of the electric potential in the horizontal midplane of *A. albifrons* (Fig. 3a) obtained in an earlier study by Assad and colleagues (Assad 1997; Assad et al. 1999). The best-fit model parameters were $L_1 = 9.61$ cm, $L_2 = 0.01$ cm, $X_1 = 4.81$ cm, and $X_2 = 9.61$ cm. The parameter values and χ^2 of the fit were insensitive to changes in pole density down to 1 pole/cm. However, our model implementation uses a higher density of 10 poles/cm to minimize spatial inhomogeneities that become apparent at closer distances and higher sampling densities than were available in the empirical data set. The small value of L_2 implies that the negative set of poles can be adequately modeled by a single negative pole at the tail, while the remaining positive poles are uniformly distributed along the full length of the body. Thus, for *A. albifrons*, the more general dual line-charge

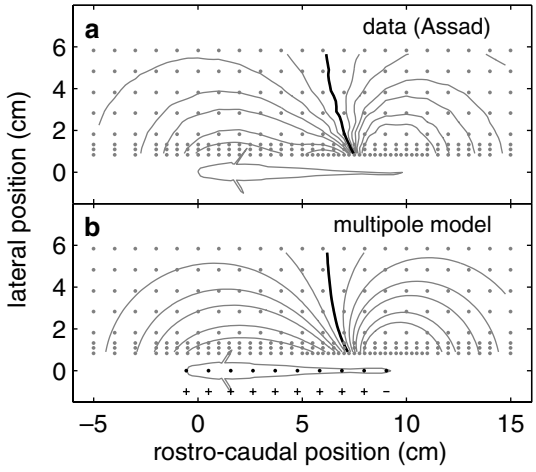

Fig. 3 Comparison of measured and modeled electric field geometry for a 9.8-cm *A. albifrons*. **a** Isopotential contours reconstructed from experimental measurements by Assad (1997). The electric potential was recorded at each of 1,580 locations (*dots*) in the horizontal midplane of the fish. The water conductivity was 210 μS/cm. **b** Modeled isopotentials using the multipole model described in Eq. 2 ($n=98$ poles, $m=1$ negative pole, $q=9.0$ mV cm, pole locations uniformly distributed along rostro-caudal body axis, with negative pole at tail). The pole density in the fish inset has been reduced by a factor of ten for clarity. The signs underneath ($\pm$) indicate pole polarity. The zero isopotential is shown in bold. Subsequent contour levels are: ± 0.25, 0.50, 0.75, 1.0, 1.5, and 2.0 mV (positive to the *left*, negative to the *right*)

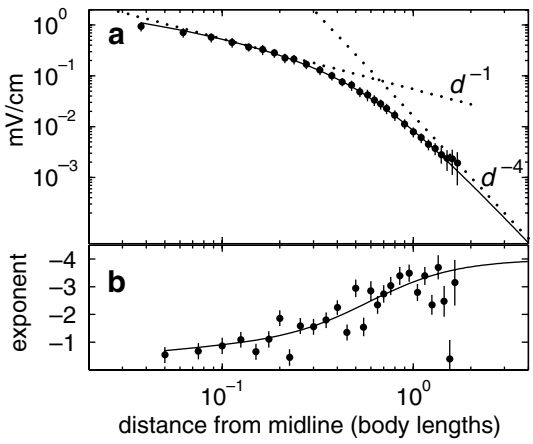

Fig. 4 Lateral *E* field versus distance. **a** Average magnitude of the lateral component of the electric field along a lateral transect starting at the midline of the trunk ($n=7$ fish, mean length 20.6 cm). The data are well described by the model (*solid line*), with a model fish length of 20 cm and an amplitude scaling factor q (Eq. 2) adjusted to fit the data ($q=14.05$ mV cm). For reference, the *dotted lines* show power-law relationships of the form of d^{-1} and d^{-4}. **b** The exponent of the local power-law relationship versus distance for the experimental data and the model (*solid line*)

model simplifies to a line-point model. The field pattern from the line-point model is elongated and weaker along the anterior portion of the fish than near the tail, in agreement with the experimental measurements (Fig. 3b). The RMS error between the model predictions and experimental measurements was 11.4% (with 47 outliers removed from 1,580 sample points).

Field strength and decay with distance

To further assess the ability of the model to accurately describe the fish's electric field, we measured and modeled the strength of the lateral component of the electric field in the trunk region (Fig. 4a). For measurements in the horizontal midplane, this is the dominant component of the electric field vector in the trunk region of the fish and has the most influence on electrosensory image formation in this region (Knudsen 1975; Rasnow and Bower 1996). The initial measurement was made with the field gradient electrode positioned next to the skin at the level of the lateral line, caudal to the operculum (at 30–40% body length), with orientation perpendicular to the skin. Subsequent measurements were taken in discrete lateral steps. The lateral field strength measured just outside the skin ranged from 0.63 mV/cm to 1.2 mV/cm with a mean of 0.97 ± 0.23 mV/cm ($n=7$). The model (Fig. 4a, solid line) is in good agreement with the data, having an RMS error of 9.1% over distances d between approximately 0.04 and 2.0 body lengths. The magnitude of the lateral *E* field changes by almost three orders of magnitude over this range of distances. The noise floor of our setup (about 1–4 μV/cm) limited the useful measurement range to approximately two body lengths.

The lateral field strength falls approximately as d^{-1} close to the fish ($d<0.2$), where d is the normalized distance from the midline in body lengths. At large distances ($d>2.0$), the falloff asymptotically approaches d^{-4}. The log-slope of the power-law decay function [log (E_{i+1})−log (E_i)]/[log (d_{i+1})−log (d_i)] has a sigmoidal dependence on d (Fig. 4b). The slope corresponds to the exponent of a local power-law relationship. The scaling varies between d^{-1} and d^{-3} over the range that is generally relevant for electrolocation-related behaviors ($d<1$).

Baseline transdermal voltage

The experimentally measured baseline transdermal voltage ranged from 0.82 to 1.90 mV, with a mean of 1.37 ± 0.41 mV ($n=7$). The transdermal recording technique potentially introduces a local current shunt at the site where the wire penetrates the skin; therefore, the reported value represents a lower bound on the actual transdermal potential in the intact animal. To normalize for any current shunting effects, most results below are reported as a percentage change in the measured baseline transdermal potential.

Background perturbations

We are interested in understanding the spatiotemporal structure of natural electrosensory images in the context

of prey-capture behavior (Nelson and MacIver 1999; MacIver et al. 2001). Weakly electric fish detect weak, prey-induced signals in the presence of much larger background perturbations. Two significant sources of electrosensory backgrounds are reafferent signals induced by changes in the geometry of the electric organ relative to the electroreceptors during tail bending (Bastian 1995), and perturbations induced by nearby nonconducting boundaries such as the water surface or large rocks in a natural setting, and aquarium walls in a laboratory environment.

Tail bending

Changes in the geometry of the electric organ relative to the electroreceptors occur during tail bending and other body movements. In general, body and tail bends toward one side of the animal tend to increase the electrosensory stimulus on that side of the body and decrease stimulation on the opposite side (Bacher 1983; Bastian 1995). We quantified the effect of tail bends as a percent change in transdermal potential on both sides of the fish as a function of bend angle. Defining positive bend angles to represent a bend towards the recording site, we pooled transdermal recordings from both the left- and right-hand sides of the body as the tail was moved through a range of ±45° (Fig. 5). The change in transdermal potential showed an approximately linear dependence on bend angle, with a slope of ≈0.05% of baseline transdermal potential per degree of bend (equivalent to 0.7 μV/deg) (Fig. 5, dashed line). This trend was reproduced by the model, although the model gave a slightly smaller slope, particularly at small bend angles (Fig. 5, solid line). The RMS error (Eq. 9) between the experiment and the model was 34.4% for angles between ±45°. One contribution to this error arises from unavoidable differences between the idealized bend geometry in the model and the actual geometry that could be achieved in the experiment by controlling only the position of the tail tip. Different bend shapes can change the nonlinearity and slope of the relationship, and can even invert the sign of the relationship for C-shaped body configurations (model data not shown). MacIver et al. (2001) reported that the RMS lateral bend angle for *A. albifrons* was 31° near the time of prey detection. Assuming a slope of 0.05% per degree of bending, this translates into a modulation in transdermal potential of about 1.5% due to lateral bending.

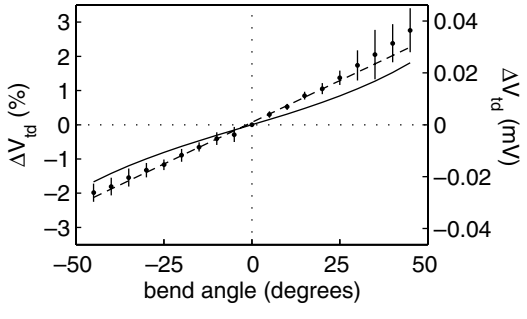

Fig. 5 Change in transdermal potential due to tail bending. Representative data from a single fish (24 cm length, recorded at 42% body length, 1.5 mV baseline transdermal potential) averaged over eight trials. The caudal-most 8 cm of the tail was bent along a circular arc while the rostral portion of the fish remained straight. The *dashed line* is a linear fit of the form ΔV_{td} (%) = 0.05 θ(deg) or equivalently ΔV_{td} (mV) = 0.075 θ(deg). The *solid line* shows the corresponding changes produced by the model

Nonconducting boundaries

The electric field of a fish swimming in its natural habitat is influenced by nonconducting boundaries that restrict the flow of electric current. Furthermore, most empirical studies of prey-capture behavior have been carried out in laboratory aquaria, where the walls and bottom surface of the tank also form nonconducting boundaries. We measured the changes in transdermal potential due to the presence of a nonconducting boundary out to a distance of 0.8 body lengths on both sides of the fish. The transdermal potential decreased on the side ipsilateral to the wall and increased on the contralateral side (Fig. 6a). The changes observed experimentally were asymmetric, reaching approximately −25% ipsilaterally and +11% contralaterally at a distance of 1.8 cm from the midline (0.09 body lengths). The magnitude of the perturbation does not follow a simple power law, but falls off approximately as d^{-2} over the range of distances tested (Fig. 6b, dashed line). The model captures the key trends of the data, although it slightly underestimates

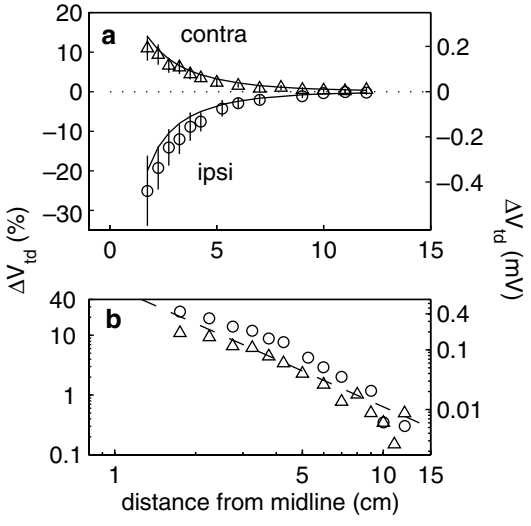

Fig. 6 Change in the transdermal potential induced by a large nonconducting boundary. **a** Changes on the ipsilateral side (*circles*) are negative and those on the contralateral side (*triangles*) are positive ($n = 5$ fish, average baseline transdermal potential of 1.75 mV). *Solid lines* show the model prediction. **b** Same data shown on a log-log scale to illustrate power-law behavior; the *dashed line* is a power law with an exponent of −2

the ipsilateral and overestimates the contralateral effect. The RMS error between the model and the experiment was 25.3 and 26.6% for ipsi- and contralateral data, respectively.

Target perturbations

Natural electrosensory scenes, such as those associated with prey capture, may include one or more small objects near the fish, such as prey, suspended debris, or small air bubbles. If these items are small compared to the fish, then the induced transdermal perturbations can be modeled by treating the object as a spherical dielectric in a locally uniform electric field (Rasnow 1996). In this section, we measure and model the changes in transdermal potential caused by spherical objects. This is similar to previous experimental work by Bastian (1981) and Rasnow (1996). To improve the signal-to-noise ratio (SNR), the objects used in our experimental studies were significantly larger than typical prey, but the model allows us to extrapolate to smaller object sizes.

Moving spheres

Objects moving relative to the fish create transient changes in transdermal potential across the surface of the skin. This transdermal perturbation has both spatial and temporal structure. Since the transdermal implant is at a fixed location for each fish, the results reported here measure only the temporal structure of the perturbation. However, the full spatiotemporal structure of the signal can be recovered from the model.

The temporal profile as the object is swept past the recording site has a center-surround structure (see Caputi et al. 1998; Gómez et al. 2004). Representative temporal profiles for metal and plastic spheres are shown in Fig. 7 for different object types (Fig. 7a, b), different distances (Fig. 7c, d), and ipsilateral versus contralateral recording sites (Fig. 7e, f). These dependencies are quantified using center and surround Gaussian parameters (Eq. 1) derived from fits of a difference-of-Gaussians function to the temporal profiles.

Image-center properties

The amplitude and width parameters of the central Gaussian were examined as a function of object type, size and distance (Fig. 8). As expected, metal spheres cause an increase in the transdermal voltage, while plastic spheres cause a decrease. The magnitude of the perturbation is dependent on object size and distance. A large sphere (1.91 cm diameter) caused roughly a 10% change in transdermal voltage at 2 cm from the fish's midline, while a small sphere (0.64 cm diameter) at the same distance caused a fraction of a percent change. The peak amplitude decays rapidly with lateral distance for both metal and plastic spheres (Fig. 8a, b). The exponent of the power-law fit averaged over all fish was -4.76 ± 0.40 ($n = 7$, see Table 1 for details). The model

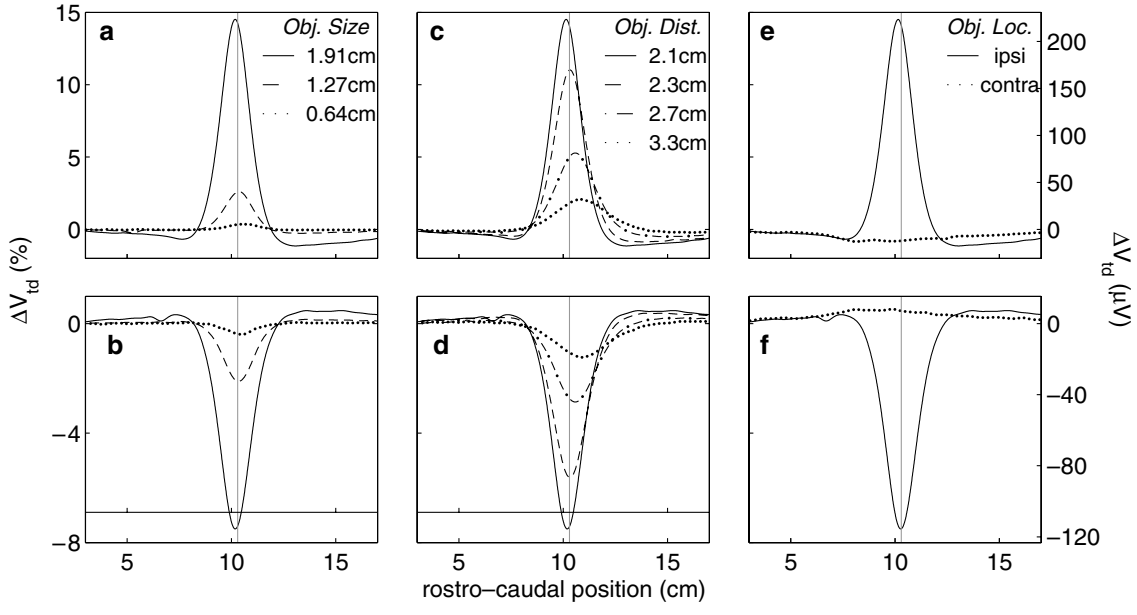

Fig. 7 Representative temporal modulation profiles for metal and plastic spheres. All recordings are from the same fish (24 cm length, recorded at 42% body length, 1.5 mV baseline transdermal potential). The objects moved parallel to the rostro-caudal axis of the fish at a constant velocity of 2.5 cm/s. The data are shown as a function of rostro-caudal object position, rather than time. The *vertical gray line* indicates the location of the recording electrode. **a**, **b** Changes with object size for **a** three metal and **b** three plastic spheres with diameters of 1.91, 1.27, and 0.635 cm (*solid*, *dashed*, and *dotted lines*, respectively) swept along the length of the fish at a fixed lateral distance of 2.1 cm from the midline. **c**, **d** Changes with object distance for a 1.91 cm diameter **c** metal and **d** plastic sphere swept along the length of the fish at lateral distances of 2.1, 2.3, 2.7, and 3.3 cm (*solid*, *dashed*, *dash-dot*, and *dotted lines*, respectively). **e**, **f** Comparison of ipsilateral (*solid lines*) and contralateral (*dotted lines*) profiles for a 1.91 cm diameter **e** metal and **f** plastic sphere at a lateral distance of 2.1 cm from the midline

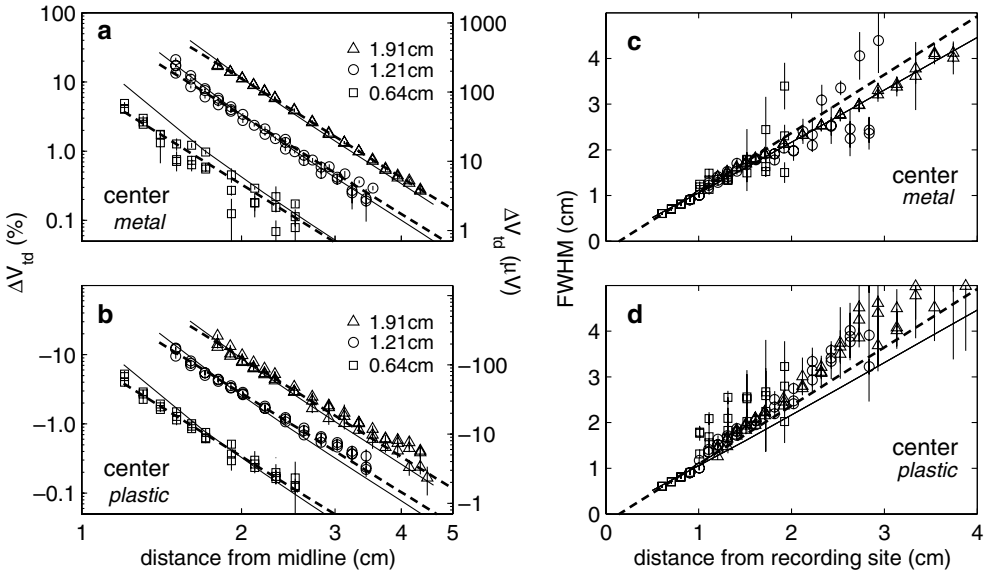

Fig. 8 Representative peak amplitudes and FWHM of the center Gaussians versus distance for a single fish (21 cm in length, recording electrode at 35% body length, 1.4 mV baseline transdermal potential). **a**, **b** Peak amplitude versus lateral distance for **a** metal and **b** plastic spheres of diameters 1.91, 1.27, 0.635 cm (*triangles*, *circles*, and *squares*, respectively) and corresponding model predictions (*solid lines*; $\chi_m = 0.55$, $\chi_p = -0.48$). The best-fit power law (*dashed lines*) has an exponent of −4.8 for this fish. **c**, **d** FWHM versus distance for **c** metal and **d** plastic spheres is shown for data and model (*solid line*). The best-fit linear relationship (*dashed lines*) is FWHM = 1.3 d_{skin} − 0.1 cm for this fish, where d_{skin} is the distance from the center of the object to the skin

shows a similar dependence (Fig. 8a, b, solid lines). The width of the center Gaussian, as characterized by the full-width at half-maximum (FWHM), varies approximately linearly with object distance for both metal and plastic spheres (Fig. 8c, d). The slope of the relationship is largely independent of object size and material (Fig. 8c, d, dashed line). The temporal profiles generated by the model have similar FWHM properties, although the slope is slightly lower in the model (Fig. 8c, d, solid line). The population best-fit parameter values for a linear fit of the form $\mathrm{FWHM} = Mx + B$ are $M = 1.16 \pm 0.09$ ($n = 7$) and $B = -0.13 \pm 0.16$ ($n = 7$) across object sizes and types. Note that x in this case is the lateral distance to the object center from the fish skin, rather than the fish midline.

The magnitude of the transdermal perturbation is expected to scale in proportion to sphere volume (a^3 in Eq. 6) and electrical contrast χ. Using the known sphere diameters, we computed the best-fit contrast values for metal and plastic objects used in these studies. We obtained values of $\chi_m = 0.92 \pm 0.55$ ($n = 7$) for metal spheres and $\chi_p = -0.74 \pm 0.35$ ($n = 7$) for plastic spheres. The theoretical values for an ideal conductor and insulator are $\chi_m = 1.0$ and $\chi_p = -0.50$, respectively (Rasnow 1996). While the mean values of χ_m and χ_p are near the expected values (within one standard deviation), the observed metal-to-plastic ratio χ_m/χ_p of -1.20 ± 0.20 ($n = 7$) does not agree with the predicted ratio of −2. Since metal electrodes in water are known to deviate from ideal conductors and effective impedance values can vary with surface cleanliness, oxidation, and movement (Robinson 1968; Rasnow 1996), we made careful control measurements quantifying the perturbation caused by clean, nonmoving metal and plastic spheres in an artificial electric field at various distances. This yielded a mean ratio for χ_m/χ_p of -1.89 ± 0.16, in agreement with the expectation of −2.0.

Image-surround properties

The amplitude and width parameters of the surround Gaussian were also examined as a function of object type, size, and distance (Fig. 9). The sign of the surround Gaussian was opposite to that of the center Gaussian: negative for metal spheres (Fig. 9a) and positive for plastic spheres (Fig. 9b). The amplitude ratio of the surround Gaussian to the center Gaussian was -0.064 ± 0.027 ($n = 805$ trials). The ratio did not depend significantly on object size or type. The population mean exponent of the power law fits for both metal and plastic (Fig. 9a, b, dashed lines) data was -4.81 ± 0.69 ($n = 7$). The population best-fit parameter values for a linear fit of the form $\mathrm{FWHM} = Mx + B$ are $M = 2.83 \pm 1.03$ and $B = 4.90 \pm 1.11$ ($n = 3$). The model produces "surround" effects that are more asymmetric than typically observed in the data, with little or no surround component on the caudal side of the image. Difference-of-Gaussian fits to the surround in the model (Fig. 9a, b, solid lines) result in smaller magnitudes and narrower widths in comparison to the data.

Contralateral-Gaussian properties

Objects close to the fish also affect the transdermal potential on the contralateral side of the body. The temporal profile recorded on the contralateral side is

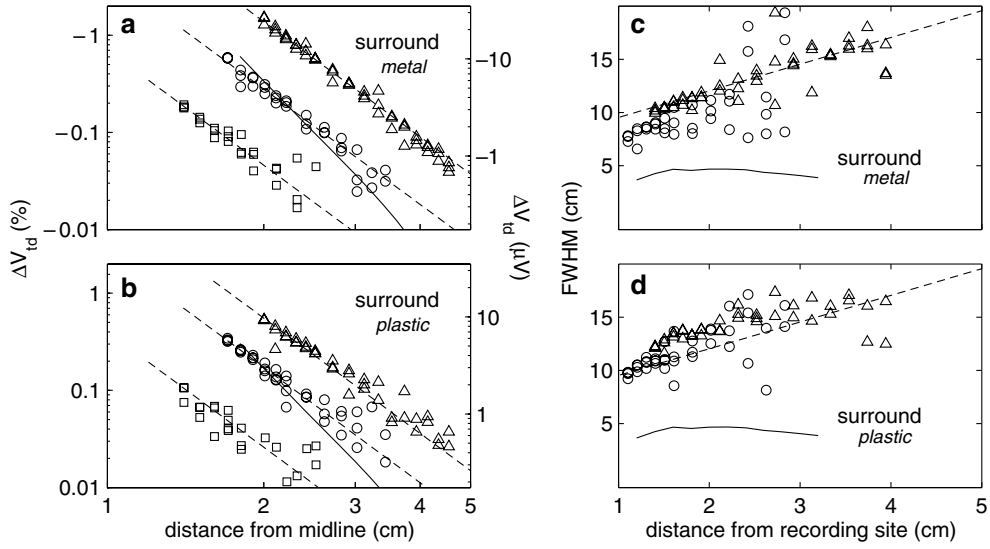

Fig. 9 Representative peak amplitudes and FWHM of the surround Gaussians versus distance for a single fish (24 cm length, recording at 42% body length, 1.5 mV baseline transdermal potential). **a**, **b** Peak amplitude versus lateral distance for **a** metal and **b** plastic spheres of diameters 1.91, 1.27, and 0.635 cm (*triangles*, *circles*, and *squares*, respectively). The model shows the corresponding relationship for a 1.91 cm diameter sphere (*solid line*; $\chi_m = 0.62$, $\chi_p = -0.52$). The best-fit power law (*dashed lines*) has an exponent of -3.9 for this fish. **c**, **d** FWHM versus distance for **c** metal and **d** plastic spheres is shown for data and model (*solid line*). The best-fit linear relationship (*dashed lines*) is FWHM = 2.5 d_{skin} + 7.0 cm for this fish

Fig. 10 Representative peak amplitudes and FWHM of the contralateral Gaussians versus distance for a single fish (24 cm length, recording at 42% body length, 1.5 mV baseline transdermal potential). **a**, **b** Peak amplitude versus lateral distance for **a** metal and **b** plastic spheres of diameters 1.91, 1.27, and 0.635 cm (*triangles*, *circles*, and *squares*, respectively). The model shows the corresponding relationship for a 1.91 cm diameter sphere (*solid line*; $\chi_m = 0.62$, $\chi_p = -0.52$). The best-fit power law (*dashed lines*) has an exponent of -2.8 for this fish. **c**, **d** FWHM versus distance for **c** metal and **d** plastic spheres is shown for data and model (*solid lines*). The best-fit linear relationship (*dashed lines*) is FWHM = 0.9 d_{skin} + 6.8 cm for this fish

weaker, broader and opposite in sign to that of the ipsilateral center peak. Metal spheres caused a decrease in contralateral transdermal voltage, while plastic spheres caused an increase (Fig. 10a, b). The contralateral peak and FWHM were fit by a single Gaussian, because no appreciable surround was discernible. The amplitude ratio of the contralateral Gaussian to the ipsilateral center Gaussian was -0.072 ± 0.041 ($n = 515$ trials). The ratio did not depend significantly on object size or type. The population mean exponent of the power-law fits for peak amplitude versus distance for both metal and plastic spheres was -3.64 ± 0.64 ($n = 4$) (dashed lines). The contralateral FWHM was significantly larger than that on the ipsilateral side, and was only weakly dependent on object distance (Fig. 10c, d). The population best-fit parameter values for a linear fit of the form FWHM = $Mx + B$ are $M = 0.46 \pm 0.65$ and $B = 8.62 \pm 1.07$ ($n = 2$). This implies that the contralateral perturbations are broad and relatively independent of target distance. The model generates contralateral profiles that are stronger and narrower than the actual data

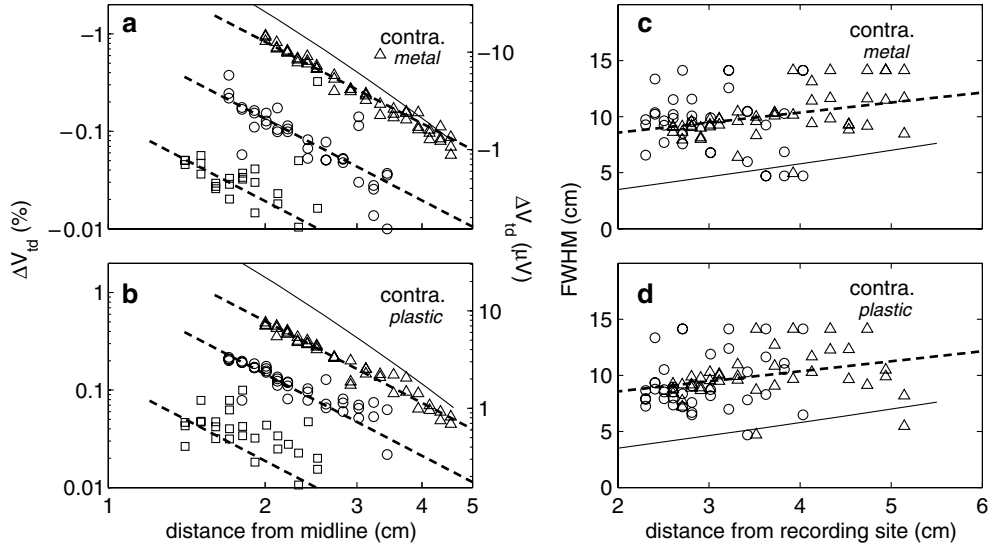

(Fig. 10a, b; solid lines). The difference between the data and the model is likely due to the low internal resistance of the fish body, which is not explicitly included in the model.

Summary of sphere effects

Table 1 summarizes the parameters of the power-law fits to peak amplitude versus distance shown in Figs. 8, 9, 10 (center, surround, and contralateral, respectively). Two fit results are reported for the center data. The row labeled "center (adj)" takes into account small systematic offsets in the lateral position of the recording electrode relative to the recording site (see Methods), which varied slightly from fish to fish. The adjustment does not significantly influence the mean values of the fits, but it significantly reduces their variance. Adjusted values are not reported for the surround and contralateral fits, because the offset adjustment had only a slight effect on parameter variance for these weaker signals.

For the center component, we also computed ratios of amplitude parameters from the power-law fits for different object sizes. For objects with the same electrical contrast (e.g., metal or plastic), the amplitude ratio is expected to scale as the cube of the ratio of diameters (Rasnow 1996). The ratios that we observed experimentally were consistent with this prediction (Table 2). Based on this scaling relationship, we can construct a generalized power-law relationship for estimating the peak amplitude of the center component as a function of object size, distance, and electrical contrast:

$$A_c(\%) \approx 670 a^3 \chi d_{\text{mid}}^{-4.8}, \tag{10}$$

where $A_c(\%)$ is the percent change in baseline transdermal voltage, a the object radius (cm), χ the electrical contrast ($-0.5 \leq \chi \leq 1$), and d_{mid} is the distance from the center of the object to the fish midline (cm). Taking a representative baseline transdermal potential of 1.4 mV, this can also be expressed as

$$A_c(\text{mV}) \approx 9.4 a^3 \chi d_{\text{mid}}^{-4.8}, \tag{11}$$

where $A_c(\text{mV})$ is the amplitude in millivolts. The corresponding surround and contralateral amplitudes would be about 5% of this value. For example, a *Daphnia* with a radius a of 0.15 cm, an electrical contrast χ of 0.6 (Nelson et al. 2002), and a distance from the midline d_{mid} of 2.0 cm, is predicted to cause a peak change in the baseline transdermal potential of 0.05% or about 0.7 μV, with surround and contralateral amplitudes less than 0.04 μV.

The spatial extent of the center Gaussian can be estimated from

$$\text{FWHM}_{\text{center}}(\text{cm}) \approx 1.2 d_{\text{skin}} - 0.1\,\text{cm}, \tag{12}$$

where d_{skin} is the distance from the object center to the receptor surface. Due to the thickness of the fish body, the distance to the skin is typically about 0.6 cm less than the distance to the midline: $d_{\text{skin}} \approx d_{\text{mid}} - 0.6$ cm. This FWHM value applies only to the rostro-caudal extent of the image in the mid-trunk region of the fish (head and tail regions are more complex). The dorso-ventral extent of the image would tend to be more restricted due to the limited height of the fish body (typically $\approx$4 cm) and influences of body curvature. The surround and contralateral components tend to be broader with FWHM values in the range of approximately one-third to one-half the length of the fish (Figs. 9c, d, 10c, d).

Table 2 Summary of amplitude ratios for different object size combinations ($n = 7$ fish for 1.91 and 1.27 cm spheres, $n = 3$ fish for 0.635 cm spheres)

Amplitude ratio	$A_{1.91}$:$A_{1.27}$	$A_{1.27}$:$A_{0.635}$	$A_{1.91}$:$A_{0.635}$
Theoretical	3.375	8.000	27.000
Center (expt.)	3.9 ± 0.8	9.0 ± 2.0	35 ± 8
Surround (expt.)	3.7 ± 1.1	8.5 ± 3.4	28 ± 9
Contralateral (expt.)	4.4 ± 2.0	7.9 ± 2.6	46 ± 35

The amplitude ratios are expected to scale as the cube of the ratio of diameters (Rasnow 1996), as shown in the top row labeled "theoretical". Ratios are first computed for metal and plastic spheres separately and then combined into a grand average for each category (center, surround, and contralateral)

Discussion

We have introduced a model of electric field generation and electrosensory image formation that allows rapid computation of electrosensory images in naturalistic settings. The model incorporates the effects of small objects, nonconducting boundaries and body movements in a unified framework. The data comparisons presented thus far have illustrated the ability of the model to reproduce transdermal voltage modulations at one or two individual points on the skin, but the model also allows electrosensory images to be rapidly computed over the entire body surface of the fish. For example, computing the change in transdermal potential at the 2,020 vertices of the polygon fish model shown in Fig. 11 a requires only a fraction of a second on a desktop PC workstation running MATLAB (2 GHz processor, 512 MB RAM).

The fast execution time should make it practical to reconstruct extended spatiotemporal image sequences experienced by a freely swimming fish, based on video tracking of its movement trajectories (MacIver and Nelson 2000). To illustrate the feasibility of this approach, we modeled the change in transdermal potential that a fish might experience during a 30-s trial in a simulated environment similar to that used in previous prey-capture experiments (Nelson and MacIver 1999; MacIver et al. 2001). A model fish was moved through a simple environment consisting of the four side walls of an aquarium and a single spherical object (Fig. 11b). The simulated transdermal potential recorded at a point along the trunk during an artificial movement

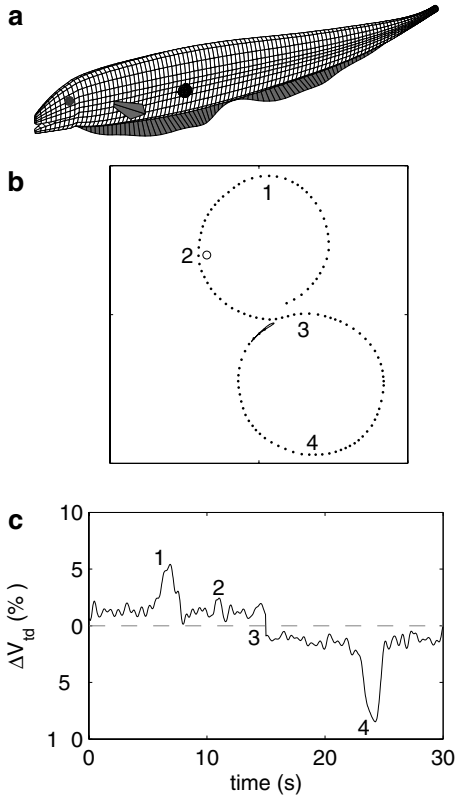

Fig. 11 Simulated transdermal potential modulations for a free-swimming fish. **a** A wireframe model of the fish body (2,020 nodes). The *black dot* on the lateral trunk indicates the transdermal recording site. **b** A simulated fish trajectory in a 100×100 cm arena with nonconducting boundaries (*solid lines* around the border). The trajectory (*dotted line*) begins near the center of the arena; *numbers* indicate sequential key points along the trajectory: *1* approach contralateral wall, *2* approach ispilateral spherical conductor (1-cm diameter), *3* abrupt change in bend angle, *4* approach ipsilateral wall. **c** percent change in transdermal potential at the site shown in **a**. *Numbers 1–4* indicate features of the transdermal modulation envelope corresponding to the key points along the trajectory

trajectory shows a complex temporal structure (Fig. 11c). Large amplitude, long duration modulations occur as the fish approaches the tank walls (points 1 and 4). Small amplitude fluctuations are associated with tail bend effects during normal swimming movements. A step change in mean transdermal potential is observed when the fish abruptly switches turning direction (point 3). A transient prey-like signal is observed (point 2) when the fish approaches a large metal sphere (1-cm diameter, electrical contrast $\chi = 1$). For illustration purposes we used a target object that is much larger than the actual prey. A prey-like perturbation of a few microvolts (a few tenths of a percent of the baseline transdermal potential) would be lost in the background noise. The simulated recording in Fig. 11c from a single point on the skin graphically illustrates the signal processing challenge faced by the fish in extracting weak prey-related signals embedded in background noise. As discussed below, there are several strategies that the nervous system can utilize to substantially improve the SNR, including spatiotemporal filtering and reafferent noise suppression.

Comparisons with previous studies

The electric field of *Apteronotus* has been previously described and modeled as a dipole field far from the electric organ (Granath et al. 1968; Knudsen 1975). Knudsen (1975) measured the magnitude of the full electric field vector along rays originating from the null isopotential point and reported that the field strength decays as d^{-3}, as expected for a simple dipole. Using a different approach, we took measurements along a lateral transect through the trunk region, and measured only a single component (lateral) of the electric field vector. We observed that the magnitude of this component decays asymptotically as d^{-4}, which is also consistent with expectations for a simple dipole under these measurement conditions. While the far field can be adequately described by a simple dipole, our results along with earlier studies (Knudsen 1975; Rasnow and Bower 1996) have shown that the field decays more slowly in the near field. Near the trunk, we observed that the lateral *E*-field decays approximately as d^{-1}. This arises because the low internal resistance of the trunk acts as a distributed current source making the field more homogeneous and decreasing the rate of decay. Our model simulates the distributed current source, created by low internal body resistance, by arranging a set of positive charges along a line, similar to the line charge model introduced by Bacher (1983). This arrangement satisfactorily reproduces both the transition from a relatively homogeneous field in the anterior of the fish to the heterogeneous field found near the tail (Fig. 3a) and the fall-off of the lateral field gradient in the near as well as in the far field (Fig. 4).

The spherical-object-induced perturbations reported here support and extend previous results by Bastian (1981) and Rasnow (1996). There are differences among these studies in the method used to monitor the voltage change. Rasnow measured only the change in potential outside the skin, whereas we quantified the transdermal potential difference across the skin, thus incorporating changes in internal potential. Bastian (1981) also measured the potential difference between the inside and the outside of the fish. However, he used a reference electrode placed in the gut of the animal, rather than directly beneath the external electrode. Bastian's technique and our technique would be equivalent if the interior of the fish were equipotential, which is only an approximation for *Apteronotus* (Scheich and Bullock 1974; Rasnow and Bower 1996). There are also differences among these studies in the method used to quantify the distance between the fish and the object. Bastian (1981) described changes as a function of the distance from the fish skin to the surface of the object. Rasnow (1996) argued that the mathematical treatment of spherical objects is simpler if the center of the object is used instead of the

surface. Rasnow compared his experimental results using the object-center convention with those of Bastian using the object-surface convention and found they were consistent when the same convention was used for both data sets. In this paper, we followed Rasnow's convention when measuring image width versus distance, but introduced a new convention for examining the distance dependence of image amplitude. In the latter case, we measured distance from object center to the fish midline, rather than to the fish skin. We found that this resulted in better (lower χ^2) power-law fits (Fig. 8a, b). If we refit our data using the distance between fish skin and object center as in Rasnow (1996), the power-law fits are worse (larger χ^2), but the power-law exponents are consistent with those reported by Rasnow (1996) and Bastian (1981; as recomputed in Rasnow 1996). Note that the definition of distance is a matter of convention; certain conventions are more conducive to particular types of mathematical analyses or yield better empirical fits, but all are valid choices. As far as behavioral relevance is concerned, it might be appropriate for the fish to estimate the distance to the center of a small object if it were directing a prey strike at that location, whereas it might be more important to correctly judge the distance to the surface of a large object, such as a rock, in order to avoid colliding with it. Our measurements of size ratios and the effective electrical contrast of metal and plastic spheres, while somewhat variable, are also consistent with previous reports (Bastian 1981) and theoretical predictions (Rasnow 1996).

The decay rate that we observe for amplitude versus distance for the active electrosense is steeper than that associated with the passive electrosense (Brown 2002; Nelson et al. 2002). This is because the strength of the target dipole is independent of distance for the passive electrosense, whereas it falls off in proportion to the fish's electric field for the active electrosense (see Eq. 6).

A clear "Mexican-hat" shaped spatial and temporal electrosensory image has been described previously in *Gnathonemus petersii*, an African weakly electric fish with a pulse-type EOD (Caputi et al. 1998; Gómez et al. 2004). In *Apteronotus*, a surround effect was first reported by Bastian (1981), but the surround properties have not been described in detail. In general, the surround component in *Apteronotus* tends to be smaller in amplitude and broader in spatial extent than reported for *Gnathonemus*. This may be due to differences in skin resistivity between the two species. A modeling study by Caputi et al. (1998) found that the surround component becomes weaker and broader as skin resistivity is increased.

Limitations of the model

The high skin and low internal-body resistances of the fish contribute to the lateral spread of the return path current. This effect was not explicitly included in our model. Thus, the surround and contralateral effects are stronger and more focal in our model than actually observed in the data. Other modeling approaches such as finite-element, finite-difference, or boundary-element methods (Heiligenberg 1975; Hoshimiya et al. 1980; Caputi and Budelli 1995; Caputi et al. 1998; Assad et al. 1999) can explicitly represent the high-resistance skin and low-resistance internal body of the fish. The other approaches can potentially provide greater accuracy at the expense of significantly increased computation time. In particular, finite-element and finite-difference methods are computationally expensive for 3D simulations that include high resolution spatial detail of the skin, leaving the boundary-element approach (Assad et al. 1999) as the best alternative for high-accuracy fish field modeling in three dimensions. However, the calculation times reported by Assad (1997) were of the order of 1 min for a 256-node fish model (on a PowerMac 8500/120), while our calculation for a 2000-node fish model runs in a fraction of a second (benefiting from both a simpler algorithm as well as a faster computer). Despite its simplicity, our model does a good job of describing the effects of body bends, boundaries, and the central component of object images (Figs. 5, 6, 8) while qualitatively reproducing the general trends of surround and contralateral effects (Figs. 9, 10).

Temporal aspects of the EOD

One aspect of electric field generation not explicitly included in the version of the model presented here is the oscillatory activity of the electric organ. In addition to firing periodically, different segments of the *Apteronotus* electric organ fire asynchronously causing a propagation of the discharge. This results in different EOD waveforms along the length of the fish (Assad et al. 1999; Rasnow and Bower 1996; Hoshimiya et al. 1980). Here we restricted our study to modulations of the EOD at one particular phase, because our research is primarily focused on understanding the neural processing of amplitude modulations coded by P-type (probability coding) electroreceptors. In principle, oscillatory activity and waveform propagation could be added to our model by converting each of the static poles into an oscillator and introducing phase delays between them (Assad 1997; Hosimiya et al. 1980). This extension to the model would allow the calculation of temporal phase shifts induced by capacitive objects or nearby electric fields, as occurs in electrocommunication and the jamming avoidance response (Heiligenberg 1991).

Electrosensory targets and backgrounds

Electrosensory targets such as *Daphnia magna* can be modeled as small spherical objects. We estimated that the transdermal voltage perturbation induced by a nearby *Daphnia* is of the order of a tenth of a percent, consistent with previous estimates (Nelson and MacIver 1999).

Weakly electric fish are able to detect these tiny prey-induced signals against a background of much larger modulations. Large amplitude modulations occur when the fish approaches nonconducting boundaries like the water surface or submerged rocks. We measured this effect for the first time and observed changes in transdermal potential of up to 30% (Fig. 6). Another significant source of background modulations is bending of the tail or the entire body, which changes the geometry of the electric organ relative to the electroreceptors. The magnitude of these changes is in the range of a few percent of the baseline amplitude (Fig. 5; see also Bastian 1995).

Implications for electrosensory processing

The amplitude of prey-related signals at the time of detection is estimated to be on the order of a tenth of a percent of the baseline transdermal voltage. In contrast, modulations due to tail bending are on the order of 1%, and modulations due to nonconducting boundaries can be of the order of 10%. Even without the complications of additional clutter (rocks, plants, etc.) in the electrosensory scene, the SNR for prey-related signals is much less than unity. This makes the prey detection and localization an extremely challenging computational task. Fortunately there are several characteristics of the signal and background components that the fish can utilize to help solve this signal-processing problem.

One key aspect is that prey-induced perturbations are spatially localized and sweep rapidly across the sensory surface of the fish (Nelson and MacIver 1999), whereas tail-bend and boundary modulations give rise to broad spatial images that change more slowly in time. Thus prey-related signals tend to have higher-frequency components in both the spatial and temporal domains. The high-pass temporal filtering characteristics of P-type primary afferent fibers (Nelson et al. 1997) should provide an initial enhancement of the SNR. Further improvements in SNR would be expected due to differential filtering across the three tuberous maps of the hindbrain ELL, each of which has a different degree of afferent convergence and exhibits different spatiotemporal filtering properties (Shumway 1989a, b). Midbrain processing may facilitate the tracking of moving prey signals. For example, neurons that respond vigorously to moving electrosensory stimuli have been described in the optic tectum of *A. albifrons* (Bastian 1982). Midbrain representations of prey target location could potentially form part of a predictive tracking system that could tune the gain and spatiotemporal filtering properties of ELL neurons through descending feedback pathways (Bastian 1986) to optimize detection and tracking performance.

Another important feature that should improve performance is that reafferent signals due to tail bend modulations are predictable. ELL pyramidal cells are capable of suppressing the reafferent component of tail bend modulations through an anti-Hebbian form of synaptic plasticity (Bastian 1996, 1999). Descending proprioceptive and electrosensory signals to the ELL converge onto the apical dendrites of ELL pyramidal cells and contribute to the formation of a "negative image" of the afferent tail bend modulations. Suppression of predictable background components of the input further enhances the SNR for prey-related signals. Perhaps, the ability to generate and subtract central expectations of sensory input may extend to other forms of background modulation. For example, as the fish swims near the surface of the water, the spatiotemporal modulation pattern due to the nonconducting boundary could, in principle, be predicted and subtracted if the fish maintained a central representation of body position and orientation relative to the surface.

A third feature that could impact electrosensory signal processing is that the contralateral effects are qualitatively different for prey and background signals. For prey, the peak magnitude of the contralateral modulation is small (only about 5% of the ipsilateral peak). In contrast, tail bend modulations have almost equal and opposite effects on the two sides of the body (Fig. 5). Similarly, the effects of nonconducting boundaries have a contralateral strength that is slightly smaller, but comparable in magnitude to the ipsilateral effect (Fig. 6). Contralateral information is transmitted to the ipsilateral ELL by ovoid cells, which may be well suited to respond to the diffuse contralateral signals (Bastian et al. 1993). Ovoid cells respond maximally when there is opposite polarity between the two sides of the body (Bastian et al. 1993) as occurs during tail bending and when approaching nonconducting boundaries.

The hypotheses outlined above concerning potential implications for electrosensory processing need to be investigated and tested by combining detailed information about electrosensory inputs under natural conditions with neuroethologically motivated anatomical, physiological and behavioral studies. The model presented here can serve as a useful tool in this endeavor by providing a means to efficiently estimate the full spatial and temporal structure of electrosensory images in naturalistic environments.

Acknowledgements We thank C. Assad and B. Rasnow for providing the electric field measurements used in Fig. 3a, and N. Lüdtke for valuable comments and discussion. This work was supported by grants from the National Science Foundation (IBN-0078206) and the National Institute of Mental Health (R01 MH49242). All animal procedures were approved by the Animal Care and Use Committee at the University of Illinois, Urbana-Champaign, USA.

References

Assad C (1997) Electric field maps and boundary element simulations of electrolocation in weakly electric fish. PhD thesis, California Institute of Technology, Pasadena, University Microfilms Inc, Ann Arbor

Assad C, Rasnow B, Stoddard PK (1999) The electric organ discharges and electric images during electrolocation. J Exp Biol 202:1185–1193

Attneave F (1954) Some informational aspects of visual perception. Psychol Rev 61:183–193
Bacher M (1983) A new method for the simulation of electric fields, generated by electric fish, and their distortions by objects. Biol Cybern 47:51–58
Barlow HB (1961) Possible principles underlying the transformation of sensory messages. In: Rosenblith WA (ed) Sensory communication. MIT Press, Cambridge, pp 217–234
Bass AH (1986) Electric organs revisited: Evolution of a vertebrate communication and orientation organ. In: Bullock TH, Heiligenberg W (eds) Electroreception. Wiley, New York, pp 13–70
Bastian J (1981) Electrolocation. I. How electroreceptors of *Apteronotus albifrons* code for moving objects and other electrical stimuli. J Comp Physiol A 144:465–479
Bastian J (1982) Vision and electroreception: integration of sensory information in the optic tectum of the weakly electric fish *Apteronotus albifrons*. J Comp Physiol A 147:287–297
Bastian J (1986) Gain control in the electrosensory system mediated by descending inputs to the electrosensory lateral line lobe. J Neurosci 6:553–562
Bastian J (1995) Pyramidal-cell plasticity in weakly electric fish: a mechanism for attenuating responses to reafferent electrosensory inputs. J Comp Physiol A 176:63–78
Bastian J (1996) Plasticity in an electrosensory system. I. General features of a dynamic sensory filter. J Neurophysiol 76:2483–2496
Bastian J (1999) Plasiticity of feedback inputs in the apteronotid electrosensory system. J Exp Biol 202:1327–1337
Bastian J (2003) Electrolocation. In: Arbib MA (ed) The handbook of brain theory and neural networks, 2nd edn. MIT Press, Cambridge, pp 391–394
Bastian J, Courtright J, Crawford J (1993) Commissural neurons of the electrosensory lateral-line lobe of *Apteronotus leptorhynchus*: morphological and physiological characteristics. J Comp Physiol A 173:257–274
Berman NJ, Maler L (1999) Neural architecture of the electrosensory lateral line lobe: adaptations for coincidence detection, a sensory searchlight and frequency-dependent adaptive filtering. J Exp Biol 202:1243–1253
Brown BR (2002) Modeling an electrosensory landscape: behavioral and morphological optimization in elasmobranch prey capture. J Exp Biol 205:999–1007
Caputi A, Budelli R (1995) The electric image in weakly electric fish. I. A data-based model of waveform generation in *Gymnotus carapo*. J Comput Neurosci 2:131–147
Caputi AA, Budelli R, Grant K, Bell CC (1998) The electric image in weakly electric fish: physical images of resistive objects in *Gnathonemus petersii*. J Exp Biol 201:2115–2128
Dusenbery DB (1992) Sensory ecology: how organisms acquire and respond to information. WH Freeman, New York
Field DJ (1987) Relations between the statistics of natural images and the response properties of cortical cells. J Opt Soc Am A 4:2379–2394
Gabbiani F, Metzner W (1999) Encoding and processing of sensory information in neuronal spike trains. J Exp Biol 202:1267–1279
Gómez L, Budelli R, Grant K, Caputi AA (2004) Pre-receptor profile of sensory images and primary afferent neuronal representation in the mormyrid electrosensory system. J Exp Biol 207:2443–2453
Granath LP, Erskine FTI, MacCabee BS, Sachs HG (1968) Electric field measurements on a weakly electric fish. Biophysik 4:370–372
Haykin S (2001) Communication systems. Wiley, New York
Heiligenberg W (1975) Theoretical and experimental approaches to spatial aspects of electrolocation. J Comp Physiol 103:247–272
Heiligenberg W (1991) Neural nets in electric fish. MIT Press, Cambridge
Hoshimiya N, Shogen K, Matsuo T, Chichibu S (1980) The *Apteronotus* EOD field: waveform and EOD field simulation. J Comp Physiol A 135:283–290
Jackson JD (1975) Classical electrodynamics. Wiley, New York
Knudsen EI (1975) Spatial aspects of the electric fields generated by weakly electric fish. J Comp Physiol 99:103–118
Lissmann HW (1958) On the function and evolution of electric organs in fish. J Exp Biol 35:156–191
MacIver MA (2001) The computational neuroethology of weakly electric fish: body modeling, motion analysis, and sensory signal estimation. PhD Thesis. Dissertation Abstracts International B (DAI-B) 62:2625
MacIver MA, Nelson ME (2000) Body modeling and model-based tracking for neuroethology. J Neurosci Meth 95:133–143
MacIver MA, Sharabash N, Nelson ME (2001) Quantitative analysis of prey capture behavior in the weakly electric fish *Apteronotus albifrons*. J Exp Biol 204:543–557
Nelson ME, MacIver MA (1999) Prey capture in the weakly electric fish *Apteronotus albifrons*: sensory acquisition strategies and electrosensory consequences. J Exp Biol 202:1195–1203
Nelson ME, Xu Z, Payne JR (1997) Characterization and modeling of P-type electrosensory afferent responses to amplitude modulations in a wave-type electric fish. J Comp Physiol A 181:532–544
Nelson ME, MacIver MA, Coombs S (2002) Modeling electrosensory and mechanosensory images during the predatory behavior of weakly electric fish. Brain Behav Evol 59:199–210
Rasnow B (1996) The effects of simple objects on the electric field of *Apteronotus*. J Comp Physiol A 178:397–411
Rasnow B, Bower JM (1996) The electric organ discharges of the gymnotiform fishes: I. *Apteronotus leptorhynchus*. J Comp Physiol A 178:383–396
Rieke F, Bodnar DA, Bialek W (1995) Naturalistic stimuli increase the rate and efficiency of information transmission by primary auditory afferents. Proc R Soc Lond B 262:259–265
Robinson DA (1968) The electrical properties of metal microelectrodes. Proc IEEE 56:1065–1071
Ruderman DL, Bialek W (1994) Statistics of natural images: scaling in the woods. Phys Rev Lett 73:814–817
Scheich H, Bullock TH (1974) The detection of electric fields from electric organs. In: Fessard F (ed) Electroreceptors and other specialized receptors in lower vertebrates. Springer, Berlin Heidelberg New York, pp 201–256
Shumway CA (1989a) Multiple electrosensory maps in the medulla of weakly electric gymnotiform fish. I. Physiological differences. J Neurosci 9:4388–4399
Shumway CA (1989b) Multiple electrosensory maps in the medulla of weakly electric gymnotiform fish. II. Anatomical differences. J Neurosci 9:4400–4415
Zakon HH (1986) The electroreceptive periphery. In: Bullock TH, Heiligenberg W (eds) Electroreception. Wiley, New York, pp 103–156